RSC Advances

PAPER

View Article Online
View Journal | View Issue

Cite this: *RSC Adv.*, 2026, **16**, 22763

Development of semicarbazide-based fluorene as an AIE-active fluorescent sensor for Cu^{2+} ions: a validation through experimental and DFT studies

Qudsia Sajid,†[a] Mahnoor Manzoor,†[a] Alam Shabbir,[a] Asad Muhammad Khan,[a] Mohammed A. Assiri,[bc] Umar Farooq*[a] and Sohail Anjum Shahzad*[a]

Received 9th March 2026
Accepted 14th April 2026

DOI: 10.1039/d6ra02022d

rsc.li/rsc-advances

A fluorene-based fluorescent sensor, **FHT**, was rationally designed and synthesized, which exhibited prominent solvatochromic behavior and aggregation-induced emission (AIE) effects in aqueous medium. Upon aggregation, the **FHT** sensor showed an enhancement in emission intensity accompanied by a bathochromic shift, indicating the formation of J-aggregates. Owing to its unique photophysical properties, **FHT** was developed as a highly selective fluorescent sensor for Cu^{2+}. Selective binding of **FHT** to Cu^{2+} resulted in significant fluorescence quenching *via* a photo-induced electron transfer (PET) process. The binding interactions of **FHT** with Cu^{2+} were studied in detail by ^1H NMR titration, liquid chromatography-mass spectrometry (LC-MS), dynamic light scattering (DLS), Fourier-transform infrared (FTIR) spectroscopy, and density functional theory (DFT) analysis. Upon interaction with Cu^{2+}, the **FHT** sensor exhibited strong fluorescence quenching with a low detection limit of 82 nM and quenching efficiency of 97%. In addition to its solution-phase sensing capability, **FHT** demonstrated effective performance in the solid state and enabled naked-eye colorimetric identification of Cu^{2+}. Furthermore, the **FHT** sensor was successfully integrated into molecular logic-gate operations, emphasizing its promise for on-site environmental monitoring and the development of molecular electronic devices.

1. Introduction

In recent years, substantial interest has been directed toward the development of highly selective and sensitive fluorescent imaging tools for the detection of transition-metal ions, resulting in great progress in the design of metal-specific fluorescent sensors.[1,2] Among these transition metals, copper has become particularly important as a target because of its important role in a large number of biological, environmental and industrial processes.[3–5] Being a redox-active species, it is involved in enzymatic processes that are essential for life, including respiration in mitochondria, biosynthesis of neurotransmitters and antioxidant defense mechanisms.[6–9] Although it is biologically important, an excess of copper may cause disruption of the homeostasis of cells, leading to severe pathological conditions.[10] Excess Cu^{2+} has been associated with Wilson's disease,[11] Alzheimer's disease,[12] Parkinson's disease,[13] and other forms of neurodegenerative diseases.[14] On the other hand, a deficiency of Cu^{2+} can cause anemia, poor immunity, and metabolic disorders.[15–17] In addition to biological concerns, Cu^{2+} is released into environmental water bodies through domestic, industrial, and agricultural activities, particularly through the use of copper-based pesticides employed to prevent plant diseases and enhance agricultural productivity.[18,19] As a result, reliable monitoring of Cu^{2+} levels in water is crucial, with guideline values set at 2.0 ppm by the World Health Organization and 1.3 ppm by the U.S. Environmental Protection Agency.[20,21] Thus, the accurate and sensitive detection of Cu^{2+} is essential to study its biological roles as well as for analyzing environmental and physiological samples.

The reported analytical techniques for Cu^{2+} sensing are atomic absorption spectroscopy (AAS),[22] inductively coupled plasma mass spectrometry (ICP-MS),[23] gas chromatography and liquid chromatography mass spectrometry,[23,24] potentiometry,[25] electrochemical techniques,[26] colorimetry,[27] and spectrophotometry.[28] However, these analytical methods face challenges, including low accuracy, poor qualitative performance, and time-consuming and high-cost instrumentation, which prevent their practical application. In contrast, fluorescence-based sensing has been developed as a powerful method for metal-ion sensing due to its low cost, high sensitivity, low detection limits, rapid response, ease of operation, and the non-invasive nature of detection.

Considering their effectiveness and extraordinary characteristics, various fluorescence sensors, including polymers,[29] carbon

[a]*Department of Chemistry, COMSATS University Islamabad, Abbottabad Campus, University Road, Abbottabad 22060, Pakistan. E-mail: umarf@cuiatd.edu.pk; sashahzad@cuiatd.edu.pk*

[b]*Department of Chemistry, Faculty of Science, King Khalid University, P. O. Box 9004, Abha 61413, Saudi Arabia*

[c]*Central Labs, King Khalid University, P. O. Box 960, Abha, AlQura'a, 61413, Saudi Arabia*

† These authors contributed equally to this work.

dots,[30] and quantum dots,[31] and small organic molecules such as rhodamine semicarbazide,[32] coumarin-based semicarbazide,[33] Schiff-based semicarbazide derivatives,[34] and naphthalimide-based semicarbazide chemosensors, have been reported for sensing of Cu^{2+}. However, these reported sensors also have drawbacks, such as high detection limits, synthetic complexity, poor selectivity, and poor stability. One factor that limits their performance is aggregation-caused quenching (ACQ), which arises due to the planar molecular geometries that result in the formation of strong intermolecular non-covalent interactions, particularly π–π stacking and dipole–dipole interactions.[35] The principle of aggregation-induced emission (AIE), which is opposite to aggregation-caused quenching (ACQ), was first reported by Tang's research group.[36] AIE-active luminogens are fluorophores that show negligible emission when diluted but present a remarkable enhancement in emission intensity in the aggregated or solid state.[37–39] The formation of molecular aggregates, such as J-aggregates, from a head-to-tail molecular alignment, which restricts intramolecular motions within the fluorophores and facilitates a more efficient radiative decay pathway.[40–42] In contrast, H-aggregates are formed through face-to-face stacking of molecules, resulting in strong excitonic coupling that leads to a blueshift (hypsochromic shift) in the emission spectra,[43] while X-aggregates exhibit a cross-stacked or twisted molecular packing pattern, leading to strong fluorescence in the solid state due to reduced non-radiative decay pathways.[44]

In this study, a fluorene-based fluorescent sensor **FHT** was synthesized through a Schiff-base condensation reaction and subsequently characterized by NMR spectroscopy and mass spectrometry. The sensor **FHT** exhibited pronounced solvatochromism, and it exhibits significant changes in emission wavelength with variation in solvent polarity, which reflects changes in its electronic distribution and stabilization in excited state. Moreover, aggregation-induced emission (AIE) was also observed in the **FHT** sensor, which was attributed to the restricted intramolecular motions (RIR) and the formation of J-aggregates, leading to an increase in the emission intensity accompanied by a bathochromic shift. Owing to its unique photophysical characteristics, the **FHT** sensor is capable of selectively and sensitively detecting Cu^{2+} through a PET mechanism in a DMF/water (1 : 9, v/v) system with a calculated LOD of 82 nM and quenching efficiency of 97%. Additionally, the **FHT** sensor was demonstrated to have good stability in different environmental conditions, such as varying pH and temperature, and is resistant to prolonged UV exposure. The **FHT** sensor was synthesized in good yield, exhibited excellent photophysical properties, including solvatochromic behavior and aggregation-induced emission (AIE). It selectiviely detects Cu^{2+} in both the solution and solid phase, while demonstrate potential for applications in molecular logic-gate systems.

2. Experimental section

2.1. Materials and chemicals

Analytical-grade reagents were utilized throughout the study and were purchased from Alfa Aesar (UK), Sigma-Aldrich (USA), Oakwood Chemicals (USA), and Daejung Chemicals & Metals (Korea). Reagents, such as acetonitrile (HPLC grade), chloroform (HPLC grade), ethanol (HPLC grade), hexane (analytical grade), DMSO (analytical grade), DMF (HPLC grade), ethyl acetate (freshly distilled), acetic acid glacial (99–110%), calcium chloride (95%), sodium carbonate (99%), sodium sulfate (99%), copper(II) nitrate (99%), nickel(II) nitrate (99%), copper cyanide (99%), and mercury(II) chloride (99%), were obtained from Daejung Chemicals & Metals (Korea). Aluminum(III) chloride (99%), potassium iodide (99%), zinc(II) sulphate (99%), silver nitrate (99%), magnesium(II) bromide (99%), fluorene (99%) and thiosemicarbazide (99%) were purchased from Oakwood, USA, and ammonium nitrate was obtained from Sigma-Aldrich. Moreover, the structure of the synthesized **FHT** sensor was confirmed using ^{1}H and $^{13}C\{^{1}H\}$ NMR spectroscopy with a Bruker Avance III spectrometer, with dimethyl sulfoxide (DMSO-d_6) employed as the solvent. Photoluminescence measurements were performed on a PerkinElmer LS-45 spectrofluorometer (Hitachi, Japan), using 340 nm as the excitation wavelength and 440 nm as the emission maximum.

2.2. Synthesis of 2-(9*H*-fluoren-9-ylidene)hydrazine-1-carbothioamide

The target compound 2-(9*H*-fluoren-9-ylidene)hydrazine-1-carbothioamide (**FHT**) was synthesized from the reaction between 9*H*-fluorenone and thiosemicarbazide by refluxing equimolar amounts (3.0 mmol) of 9-fluorenone **1** and thiosemicarbazide **2** in 10 mL of absolute ethanol with 2–3 drops of glacial acetic acid as a catalyst. Reaction progress was monitored using TLC with the R_f value of 0.45; after completion, the mixture was cooled to ambient temperature, and the precipitate was isolated by filtration. Purification by silica gel column chromatography (eluent : *n*-hexane/ethyl acetate, 1 : 1) gave the desired pure product as a yellow powder (547 mg, 72% yield). The melting point of the synthesized compound **FHT** was 189 °C. ^{1}H NMR (400 MHz, DMSO-d_6) (δ, ppm): 10.84 (s, 1H NH), 8.73 (s, 1H, NH), 8.43 (s, 1H, NH), 8.04 (dd, $J = 7.4$, 0.9 Hz, 2H, ArH), 7.89 (d, $J = 7.6$, 0.9 Hz, 1H, ArH), 7.81 (d, $J = 7.6$, 0.9 Hz, 1H, ArH), 7.52 (td, $J = 7.6$, 1.0 Hz, 1H, ArH), 7.43 (dd, $J = 7.4$, 1.2 Hz, 2H, ArH), 7.34 (td, $J = 7.5$, 1.1 Hz, 1H, ArH). $^{13}C\{^{1}H\}$ (100 MHz, DMSO-d_6) (δ, ppm): 180.61 (1 × C), 145.93 (1 × C), 141.89 (1 × C), 139.80 (1 × C), 137.08 (1 × C), 131.74 (1 × C), 130.72 (1 × C), 129.56 (1 × C), 128.57 (1 × C), 128.52 (1 × C), 127.69 (1 × C), 122.86 (1 × C), 121.15 (1 × C), 120.66 (1 × C). DEPT-135 NMR (100 MHz, DMSO-d_6): (δ, ppm): 131.74 (1 × C), 130.72 (1 × C), 128.57 (1 × C), 128.52 (1 × C), 127.69 (1 × C), 122.86 (1 × C), 121.15 (1 × C), 120.66 (1 × C).

2.3. Fluorescence experiments

For fluorescence emission experiments, an optimized concentration of 30 μM of the **FHT** sensor was utilized in a DMF/H_2O solvent system with a 1 : 9 (v/v) ratio. 30 μM of sensor **FHT** exhibited enhanced fluorescence intensity upon excitation at 340 nm. Sensor **FHT** exhibited a strong fluorescence emission peak at 440 nm without self-quenching or inner filter effect (Fig. S1a). A slight decrease in emission was observed with futher increase in concentration from 30 to 50 μM, likely due to the inner filter effect; therefore, an **FHT** concentration of 30 μM

was selected for all subsequent sensing studies to ensure optimal sensitivity and reproducibility. The fluorescence behavior of the **FHT** sensor was also investigated by gradually changing the water content from 0 to 90% in dimethylformamide (DMF) to determine the solvent-dependent emission properties. Similarly, 1 mM stock solutions of different metal salts, such as calcium chloride, sodium carbonate, sodium sulfate, copper(II) nitrate trihydrate, nickel(II) nitrate hexahydrate, copper(I) cyanide, mercury chloride, aluminum chloride, ammonium nitrate, potassium iodide, zinc sulphate, silver nitrate, magnesium sulphate, and ammonium nitrate, were prepared, and each was added separately to the optimized **FHT** sensor solution in DMF/H_2O (1 : 9, v/v). In order to assess the effect of metal ions on the **FHT** sensor, fluorescence titrations were conducted by adding the metal ions gradually and tracking the variation in emission intensity.

2.4. Computational methodologies

Density functional theory (DFT) and similar theoretical calculations were performed with the Gaussian 09 program package.[45] GaussView 5.0, VMD, Multiwfn 3.7 and GaussSum were used to process and visualize the computational output data, to facilitate their analysis. The B3LYP functional (Becke's three-parameter exchange with Lee–Yang–Parr correlation) was employed for geometry optimization of the **FHT** sensor and **FHT**–Cu^{2+}, and the ωB97XD functional was utilized for calculating the interaction energy of the **FHT** sensor with Cu^{2+} for long-range and unique dispersion interactions.[46] The Pople-type basis set 6-311G(d,p), corresponding to a triple-zeta level with added polarization functions, was employed to calculate the electronic structure and molecular properties of the **FHT** sensor, while the LanL2DZ basis set, due to its effective core potential, was utilized for **FHT**–Cu^{2+}, being suitable for transition-metal complexes and organometallics.[47,48] These kinds of computation approaches are well known to provide a reliable description of molecular geometries and non-covalent interactions. In addition, frontier molecular orbital (FMO) and density of states (DOS) analyses based on Gaussian 09 were performed to give information about the electronic features of the interacting molecules.[49] Multiwfn and VMD were used to study the non-covalent interactions, which offered an understanding of van der Waals, electrostatic and steric repulsive interactions between the fragments.[50] This NCI analysis was conducted by investigating 2D reduced density gradient (RDG) space and 3D isosurface displays.[51] Furthermore, QTAIM analysis, according to Bader's theory, was carried out to elucidate the nature and strength of the interactions between the sensor and the analyte.[52]

3. Results and discussion

3.1. Chemistry of the FHT sensor

The synthesis of the **FHT** sensor was achieved *via* a Schiff-base condensation reaction, wherein the carbonyl group of reactant **1** is attacked by the terminal amino group of reactant **2**. This results in the production of a C=N double bond following a dehydration phase under acidic and reflux conditions. As a result, a C=N linkage forms between the fluorenone moiety and the thiosemicarbazide group, yielding the desired product (Scheme 1). The **FHT** sensor was characterized by ^1H, ^{13}C, and DEPT-135 NMR spectroscopy. Aromatic and olefinic protons appeared between δ 7.02–7.87 ppm in the ^1H NMR spectrum (Fig. 1a). In the ^{13}C NMR spectrum, peaks at δ 180.60 ppm and 145.93 ppm correspond to thio-carbonyl (C=S) and imine (C=N) carbons, respectively (Fig. S1b). The absence of a carbonyl (C=O) signal near δ 193 ppm confirmed the formation of the imine moiety in the **FHT** sensor. The DEPT-135 NMR spectrum showed the expected carbon signals, further confirming the successful synthesis of the **FHT** sensor (Fig. S1c). Detailed NMR spectra of **FHT** are shown in the SI.

3.2. Solvatochromism

To examine the solvatochromic emission performance of the **FHT** sensor, solvents of different polarities were studied. The **FHT** sensor was found to exhibit a significant change in the emission maximum throughout its response to the solvent environment, with 410 nm in ethyl acetate, 426 nm in chloroform, 440 nm in DMF, 443 nm in ethanol, and 455 nm in acetonitrile (Fig. 1b). It is suggested that this gradual bathochromic effect of 45 nm is indicative of increased stabilization of the excited state as compared to the ground state, and it is observed that the excited state of the **FHT** sensor exhibits intramolecular charge transfer (ICT) character. The ICT mechanism is facilitated by the presence of heteroatoms (N and S) and the π-conjugation structure in the **FHT** sensor, making the excited state more sensitive to the surrounding solvent environment. The imine (–C=N–), thiocarbamide linkage (–HN–C=S), and aromatic core facilitate a powerful intramolecular charge transfer on excitation. Therefore, the ICT in excited state is more stabilized by polar solvents, resulting in bathochromic emission.[53,54] The variation in emission wavelengths of the **FHT** sensor were evaluated using the Commission Internationale de l'Eclairage (CIE) chromaticity diagram, which provides a graphical representation of emission color based on chromaticity coordinates; the emission maxima are indicated with black markers situated within the blue spectral region at coordinates (0.152, 0.162) and (0.159, 0.221) (Fig. 1c).

3.3. Aggregation-induced emission behavior of the FHT sensor in aqueous media

The solubility of organic fluorophores is generally very low in highly polar solvents such as water, and they readily aggregate in aqueous solutions. These aggregates can greatly affect the

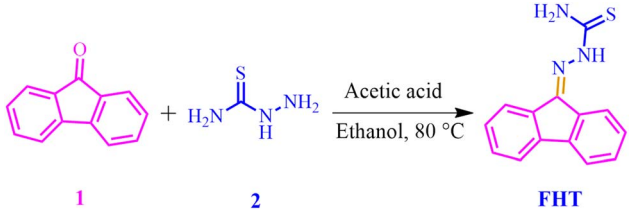

Scheme 1 Synthetic scheme to access the fluorene-based sensor FHT.

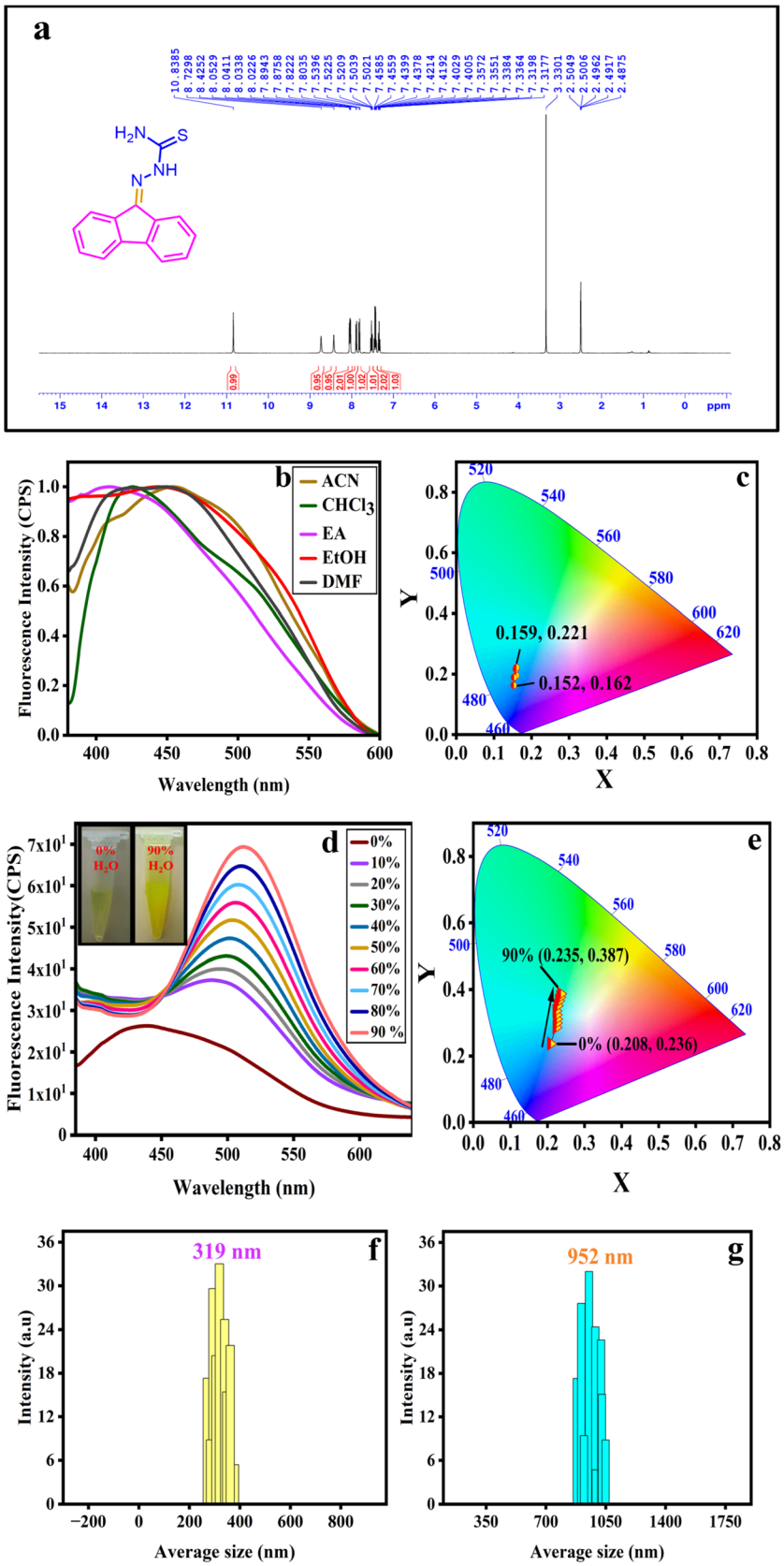

Fig. 1 ^{1}H NMR spectrum recorded in DMSO-d_6 of the FHT sensor (a). Emission spectra of the FHT sensor recorded in various solvents (excitation wavelength: 340 nm; concentration: 30 μM) (b). CIE chromaticity diagram illustrating shifts in the emission maximum (c). Emission spectra of the FHT sensor across various water fractions from 0% to 90% (d). CIE chromaticity diagram of the FHT sensor at different water fractions (e). DLS analysis performed at 0% and 90% water content to evaluate the aggregation behavior of the FHT sensor (f and g).

fluorescence emission properties of fluorophores when they are formed or dissociated. In order to examine how aggregation influences the emission characteristics of the **FHT** sensor, fluorescence spectra were measured in mixtures of DMF/H_2O with different concentrations of water between 0% and 90%. The **FHT** sensor showed a significant photoluminescence in pure DMF, and this was gradually enhanced with increasing amounts of water (0–90%). The maximum emission intensity of the **FHT** sensor was observed in 90% aqueous medium, which can be attributed to the restriction of intramolecular rotations. Moreover, a bathochromic shift of 72 nm from 440 nm to 512 nm was observed upon incremental addition of water from 0% to 90% (Fig. 1d). The redshift in the emission maximum was attributed to J-aggregate formation arising from head-to-tail molecular alignment of the **FHT** sensor due to enhanced hydrophobic interactions aligned with Kasha's rule. This rule explained that excitonic coupling within the aggregates splits the excited states, and the corresponding alteration of the ground- and excited-state energies reduces the band gap, thereby producing a large bathochromic shift and increase in emission intensity.[55,56] The color change associated with the wavelength was also depicted in the CIE chromaticity diagram. The apparent variation in the coordinates of chromaticity from (0.208, 0.236) at 0% water content to (0.235, 0.387) at 90% water content demonstrates a clear shift in the emission wavelength (Fig. 1e). DLS analysis was used to further evaluate the particle size of the **FHT** sensor. The results showed an increase in the hydrodynamic diameter from 319 nm in pure DMF to 952 nm in a 90% aqueous medium, indicating that the **FHT** sensor tends to form aggregates (Fig. 1f and g).

4. Sensing studies

4.1. Fluorescence-based detection of Cu^{2+} using the FHT sensor

To investigate the sensing capabilities of the **FHT** sensor, photophysical titration studies were carried out. For this purpose, solutions of various metal cations, including Mg^{2+}, Al^{3+}, Fe^{3+}, Cu^{2+}, Hg^{2+}, K^+, Ag^+, NH_4^+, Ni^{2+}, Zn^{2+}, Cu^+, and Na^+, were individually added to a 30 μM solution of **FHT** sensor in DMF/H_2O (1 : 9, v/v). As shown in Fig. S1d, the absorption spectrum of the **FHT** sensor exhibited a maximum wavelength at 368 nm. Upon increasing the concentration of Cu^{2+} (0–30 μM), an enhancement in the absorption band was observed, which is attributed to a π–

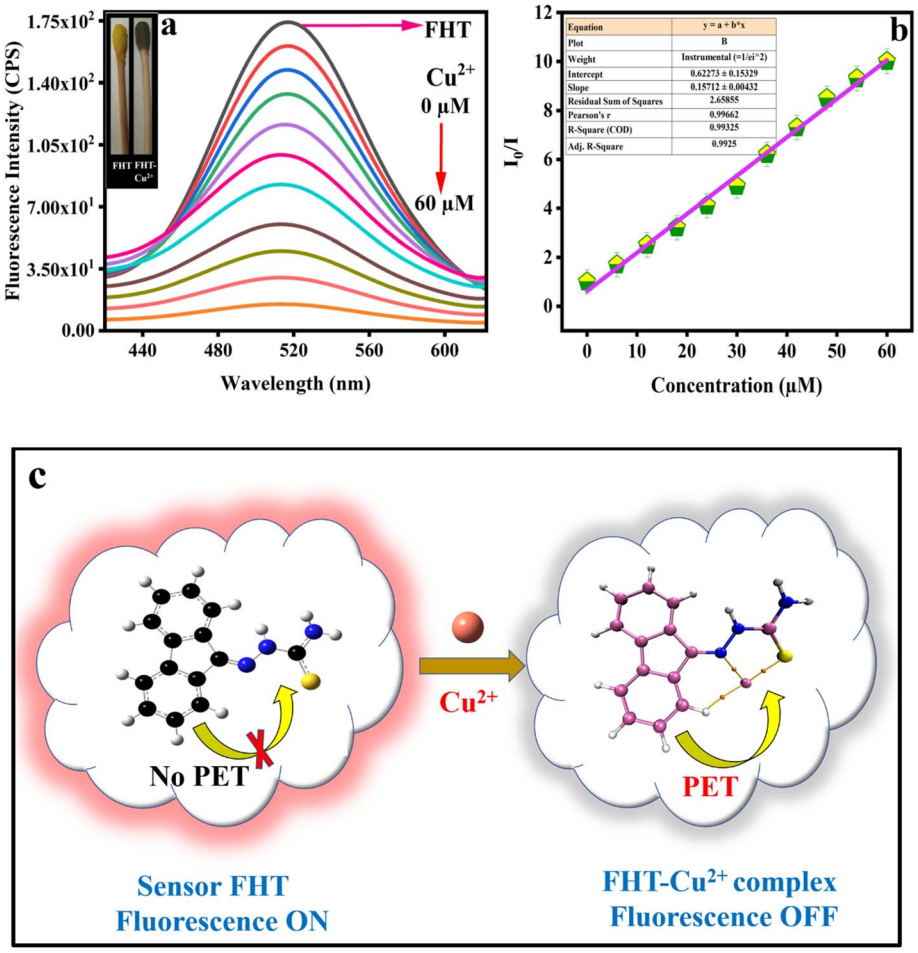

Fig. 2 Emission response of the FHT sensor to increasing concentrations of Cu^{2+} (0–60 μM) (a) inset represents the colorimetric change with and without copper. 2D Stern–Volmer plot of the FHT–Cu^{2+}complex (b). Schematic of the detection of Cu^{2+} by the FHT sensor (c).

π* transition due to the donor–acceptor framework of the **FHT** sensor. To further evaluate the sensing capacity of the **FHT** sensor, emission studies were conducted. Fluorescence measurements showed that the emission intensity of the **FHT** sensor decreased significantly in the presence of 0–60 μM Cu^{2+} (Fig. 2a). A 2D linear SV plot was plotted to measure the sensitivity of the **FHT** sensor towards Cu^{2+} (0–60 μM), which showed a remarkable quenching efficiency (QE) of 97% and a limit of detection (LOD) of 82 nM, which is significantly smaller than those of the previously tuned Cu^{2+} chemosensors (Fig. 2b and Table S1). The calculated limit of quantification (LOQ) of 275 nM is an indication of the high sensitivity of the **FHT** sensor for Cu^{2+}. The sensitivity of the **FHT** sensor was assessed by calculating the limit of detection (LOD) and quantification (LOQ) by using the formulas $3\sigma/S$ and $10\sigma/S$, where σ represents the standard deviation of the blank (0.00432), and S is the slope of the calibration curve. The LOD and LOQ were determined to be 82 nM ± 2 nM and 275 nM ± 8 nM, with a relative error of approximately 2.75%, confirming the accuracy and reproducibility of the method. To determine the metal-ion sensing behavior of the **FHT** sensor, the fluorescence response was examined using a 3D Stern–Volmer plot in the presence of other competing analytes. The analysis demonstrated a marked variation in relative fluorescence intensity (I_0/I) upon the addition of Cu^{2+} within the concentration range of 0–60 μM, but negligible changes were observed in emission intensity with other metal ions, indicating the high selectivity of the **FHT** sensor for Cu^{2+} (Fig. S1e).

4.2. Plausible mechanistic approach

The **FHT** sensor contains the fluorene moiety as a fluorophore and weakly electron-withdrawing groups such as the Schiff base (–C═N–) and urea moiety (NH–CS–NH) as receptor units. In the absence of Cu^{2+}, the **FHT** sensor exhibits pronounced fluorescence due to the lack of optimal coplanarity between the fluorene donor moiety and the receptor unit, which results in the suppression of photoinduced electron transfer (PET). Upon the addition of Cu^{2+}, the **FHT** sensor coordinates with the metal through the nitrogen and sulfur atoms of the receptor unit forming a chelated complex. The receptor unit becomes significantly more electron-deficient and geometrically suitable, with better donor–acceptor electron coupling. This structural feature favors photoinduced electron transfer (PET) from the fluorene moiety to the receptor unit. Owing to the paramagnetic character of Cu^{2+} (d^9 electronic configuration), the complex formation favors stronger intersystem crossing and non-radiative decay processes, which are responsible for the marked fluorescence quenching (Fig. 2c).[57] For this purpose, dynamic light scattering (DLS) analysis was performed to investigate the interaction of Cu^{2+} with the **FHT** sensor. Upon addition of Cu^{2+}, the hydrodynamic diameter of the **FHT** sensor increased from 952 nm to 1424 nm, indicating the formation of a stable **FHT**–Cu^{2+} complex (Fig. S2a and b). To further investigate the interaction between the **FHT** sensor and Cu^{2+}, ^1H NMR titration studies were carried out. These studies showed that a noticeable chemical shift change occurs in the ^1H NMR spectrum of the **FHT** sensor upon the addition of Cu^{2+}. As acidic protons are highly sensitive to the ionic environment, upon addition of Cu^{2+}, the local ionic environment is further altered and, most importantly, broadening of the NMR signals arises due to the paramagnetic nature of copper. The water peak observed at 3.36 ppm in the absence of Cu^{2+} is shifted downfield to 3.56 ppm after the addition of Cu^{2+}, likely due to interactions between Cu^{2+} and the **FHT** sensor. Notably, the DMSO-d_6 solvent signal at 2.49 ppm remains unchanged, indicating that the shifts in other NMR signals result from specific interactions of the **FHT**–Cu^{2+} complex (Fig. 3a). In addition, FTIR experiments were conducted to study the non-covalent interactions between the **FHT**–Cu^{2+} complex. The presence of a characteristic band at 1642 cm^{-1}, associated with the azomethine (C═N) stretching vibration, confirmed the formation of the Schiff base. The distinct band at 1056 cm^{-1} is attributed to the thiocarbonyl (C═S) mode of vibration, and an aromatic C–H vibration is observed at 3083 cm^{-1}. Upon coordination with Cu^{2+}, the C═N, C═S, and C–H bands shifted to 1637 cm^{-1}, 1050 cm^{-1}, and 3079 cm^{-1}, respectively, indicating the non-covalent interactions between the **FHT**–Cu^{2+} complex (Fig. 3b). Furthermore, mass spectrometry titration experiments were performed to investigate the interaction between sensor **FHT** and Cu^{2+}, with the m/z of $[\mathbf{FHT} + H]^+$ calculated for $[C_{14}H_{11}N_3SH]^+$: 254.07; found: 254.17 and $[\mathbf{FHT} + H + K]^+$ calculated for $[C_{14}H_{11}N_3SHK]^+$: 293.123; found: 293.33. Upon coordination of sensor **FHT** with Cu^{2+}, the values of m/z of $[(\mathbf{FHT})_2$–Cu complex$]^+$ was calculated for $C_{28}H_{22}CuN_6S_2$; calculated: 569.06, and found 569.17, respectively. The formation of this species likely arises from the reduction of Cu^{2+} during the ionization process in the ESI-MS, facilitated by the experimental conditions, possibly at higher temperatures. For d^{10} Cu(I) complexes, it is common for the metal ion to adopt a square planar geometry, in the given system, considering the weak Lewis basicity of nitrogen atoms and the strong affinity of the sulfur atoms for copper ion, favor that Cu^{2+} ion preferentially coordinates with two **FHT** molecules. The mass spectrometry titration results showed an increment in the m/z value of the **FHT** sensor upon interaction with Cu^{2+}, thereby validating the sensing of Cu^{2+} (Fig. S3a and b).

4.3. Interference studies

To analyze the selectivity of the **FHT** sensor, we conducted interference studies. For this purpose, the **FHT** sensor (30 μM) was exposed to Cu^{2+} and other analytes with concentrations ranging from 0 μM to 60 μM, such as Mg^{2+}, Al^{3+}, Fe^{3+}, Hg^{2+}, K^+, Ag^+, NH_4^+, Ni^{2+}, Zn^{2+}, Cu^+, and Na^+, and their counter anions SO_4^{2-}, Cl^-, NO_3^-, CN^-, I^-, CO_3^{2-}, Br^-, and F^- (Fig. S4a and b). Fluorescence spectral analysis indicated that the emission response of the **FHT** sensor was not significantly altered in the presence of these competing species, indicating a high level of selectivity towards Cu^{2+} (Fig. 3c). Also, the sensitivity to changing environmental conditions of the **FHT** sensor was measured by conducting fluorescence measurements in the pH range of 3–11. It was observed that the **FHT** sensor exhibited stable fluorescence intensity after binding with Cu^{2+}, irrespective of the pH of the solution, and this demonstrates the suitability of the sensor for

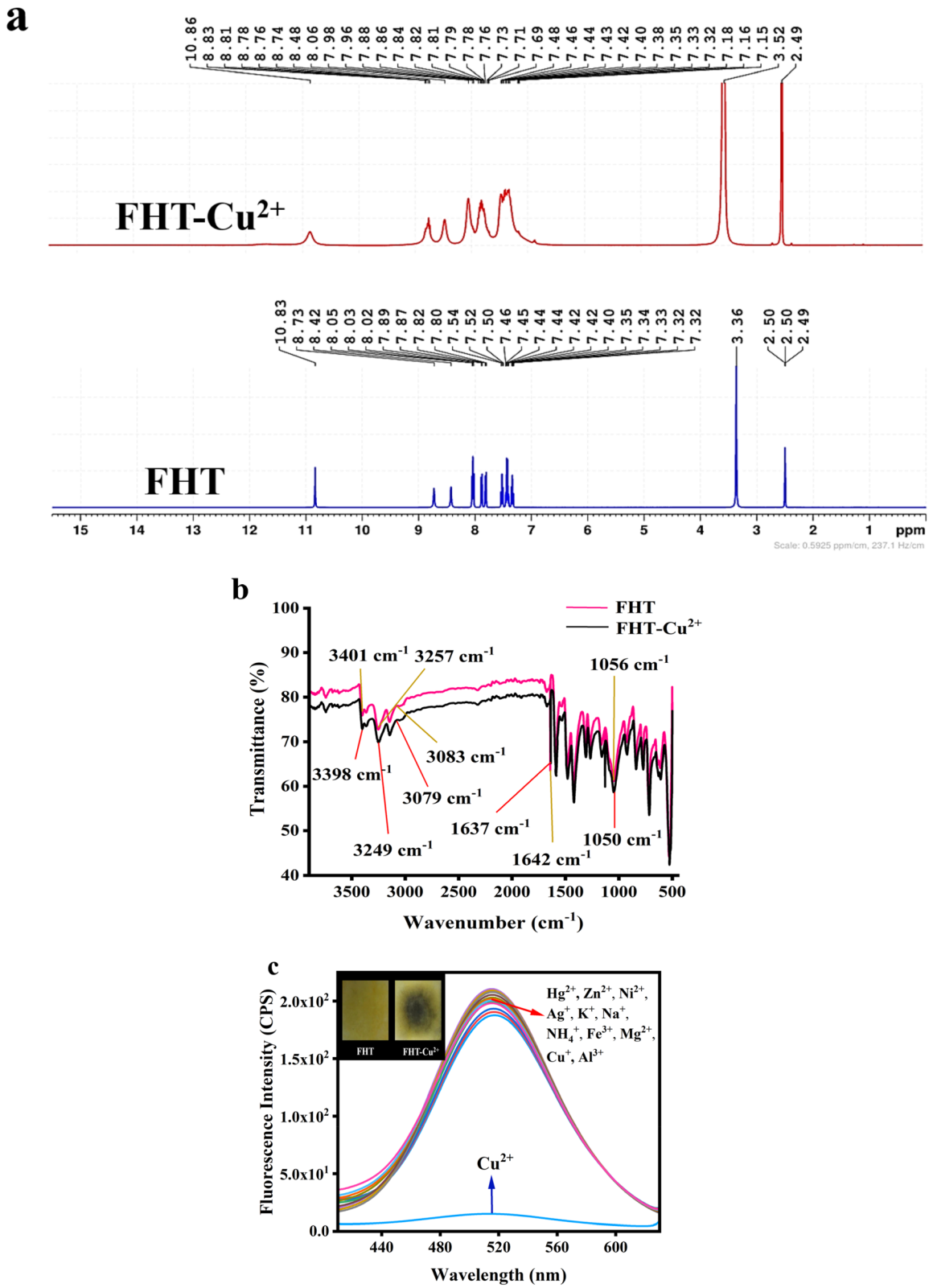

Fig. 3 Stacked ^{1}H NMR titration spectra of the **FHT** sensor and **FHT**–Cu^{2+} complex (a). Stacked FTIR titration spectra of the **FHT** sensor and **FHT**–Cu^{2+} complex (b). Emission response of the **FHT** sensor in the presence of different competing analytes (excitation wavelength = 340 nm, concentration of **FHT** sensor 30 μM in 1 : 9 v/v DMF/H_2O) inset represent the solid phase sensing with and without Cu^{2+} (c).

applications in real-life, field-based studies. These findings indicate that the **FHT** sensor can easily be used to detect Cu^{2+} within a vast pH range (Fig. S5a). In order to further assess the suitability of the **FHT** sensor, the effect of temperature on the fluorescence response was investigated in the range of 10–60 °C using a solution containing 30 μM sensor and 60 μM Cu^{2+} in DMF/H_2O (1 : 9, v/v). The fluorescence intensity of **FHT** sensor remained relatively stable across this temperature range, demonstrating the suitability of the sensor for real sample applications (Fig. S5b). Research on photostability is essential for the practical use of the **FHT** sensor. To evaluate the possible photobleaching impact, a 30 μM solution of **FHT** containing 60 μM Cu^{2+} was exposed to constant high-energy UV-irradiation, and the fluorescence emission of the solution was recorded at various time intervals. The results indicated that the **FHT** sensor exhibited a minimal change in the intensity of fluorescence with time, thereby proving that this sensor is highly photostable and resistant to photobleaching (Fig. S6a). Response time is another significant parameter to be considered for assessing the practical applicability and stability of the **FHT** sensor. One way to determine this is by measuring the quenching of the **FHT** sensor using the addition of Cu^{2+} after varying intervals (Fig. S6b). These findings demonstrated that the sensor exhibits a fast and consistent response, making it suitable for real-time detection.

5. DFT studies

5.1. FMO and DOS analysis

The sensitivity of the **FHT** sensor towards Cu^{2+} was further examined by frontier molecular orbital (FMO) analysis.[58,59] A major alteration in the electronic properties of the **FHT** sensor was observed when it interacted with Cu^{2+}. The **FHT** sensor was found to possess a HOMO–LUMO gap of 2.13 eV; however, when complexed with Cu^{2+}, the H–L gap was significantly reduced to 0.67 eV. Further, the sensitivity was validated by the density of states (DOS) analysis. A significant reduction in the HOMO–LUMO energy gap, as well as the appearance of some more virtual orbitals, was observed. The initial energy levels of the **FHT** sensor at −4.89 eV and −2.76 eV shifted to −13.03 eV and −12.36 eV after formation of the **FHT**–Cu^{2+} complex, suggesting a significant electronic interaction and enhanced sensitivity of the **FHT** sensor towards Cu^{2+} (Fig. 4a and b).

5.2. NCI and QTAIM analysis

Computational analysis *via* Multiwfn was employed to gain insight into the nature and strength of non-covalent interactions between the **FHT** sensor and Cu^{2+}.[60,61] These interactions primarily consists of hydrogen bonding, ion–dipole interactions, weak van der Waals forces, and steric repulsion. The nature of these interactions was further analyzed using 3D-isosurface representations and 2D-reduced density gradient (RDG) plots. The 3D isosurface of the **FHT**–Cu^{2+} complex provides visuals on the occurrence of the van der Waals interactions, indicated by the red patches located at the sites of interaction between the **FHT** sensor and Cu^{2+} (Fig. 4c). Dense green spikes in the 0.0102 ($2 - R$) range show that there are van der Waals interactions, and red spikes represent steric repulsion as the **FHT** sensor and Cu^{2+} interact (Fig. 4d). Meanwhile, a QTAIM analysis based on Bader's theory demonstrated that the **FHT**–Cu^{2+} complex contains 3 bond critical points (BCPs), which further validates the experimental findings of interaction between sensor **FHT** and Cu^{2+} (Fig. 4e). The **FHT**–Cu^{2+} complex has different bond critical points (BCPs) with different interactions energies; for example, BCP 1 has −1213.79, BCP 2 has −131.30, and BCP 3 has −770.51 kJ mol^{-1} (Table S2). The **FHT**–Cu^{2+} complex was found to have three BCPs, indicating Cu–H, Cu–N and Cu–S interactions, which highlight the important binding sites contributing to sensor–metal coordination.

6. Practical applications

6.1. Solid-state detection and visual sensing of Cu^{2+}

To evaluate the feasibility of the **FHT** sensor for Cu^{2+} detection, two types of solid-state sensing experiments were carried out. For this, a cotton bud was first immersed in a 30 μM **FHT** sensor solution and dried at 60 °C. Under 365 nm UV light, the sensor-coated cotton bud exhibited bright fluorescence, which was quenched upon the addition of a single drop of Cu^{2+}, producing a distinct dark spot (Fig. 2a). For additional solid-state sensing, Whatman filter paper was similarly soaked in 30 μM **FHT** sensor solution and dried. It exhibits high emission under 365 nm UV light. Upon the introduction of Cu^{2+} on these strips, the fluorescence emission of the **FHT** sensor decreased significantly. Both substrates demonstrated strong fluorescence under UV light, highlighting their potential as practical platforms for Cu^{2+} detection (Fig. 3c). To further investigate the colorimetric behavior, the **FHT** sensor was subjected to visual sensing experiments in the presence of Cu^{2+}. A 30 μM solution of the sensor in DMF/H_2O (1 : 9, v/v) exhibited bright fluorescence under 365 nm UV light. Upon addition of 60 μM Cu^{2+}, a significant decrease in fluorescence emission was observed (Fig. 4f). The results suggest that the **FHT** sensor is suitable for rapid, qualitative detection of Cu^{2+} under UV irradiation.

6.2. Industrial waste detection of Cu^{2+}

In the case of industrial wastewater, the concentration of Cu^{2+} in environmental samples is often high; therefore, its detection is necessary. Tests were conducted to assess the practical applicability of the **FHT** sensor by analyzing water samples collected from an industrial laser-cutting plant in Abbottabad, Pakistan, containing Cu^{2+} leached from copper-coated metal sheets. To minimize possible contaminants, the samples were filtered through carbon filters and then spiked with known concentrations of Cu^{2+} (0–60 μM). The spiked samples were incubated with a 30 μM solution of the **FHT** sensor in DMF/H_2O (1 : 9, v/v), and the fluorescence response was monitored using a spectrofluorometer (Fig. 4f and Table S3). Recovery efficiency was calculated from the quenching of the spiked and un-spiked samples and determined to be as high as 97%, indicating that the **FHT** sensor is suitable for the sensitive and reliable determination of Cu^{2+} in real environmental samples.

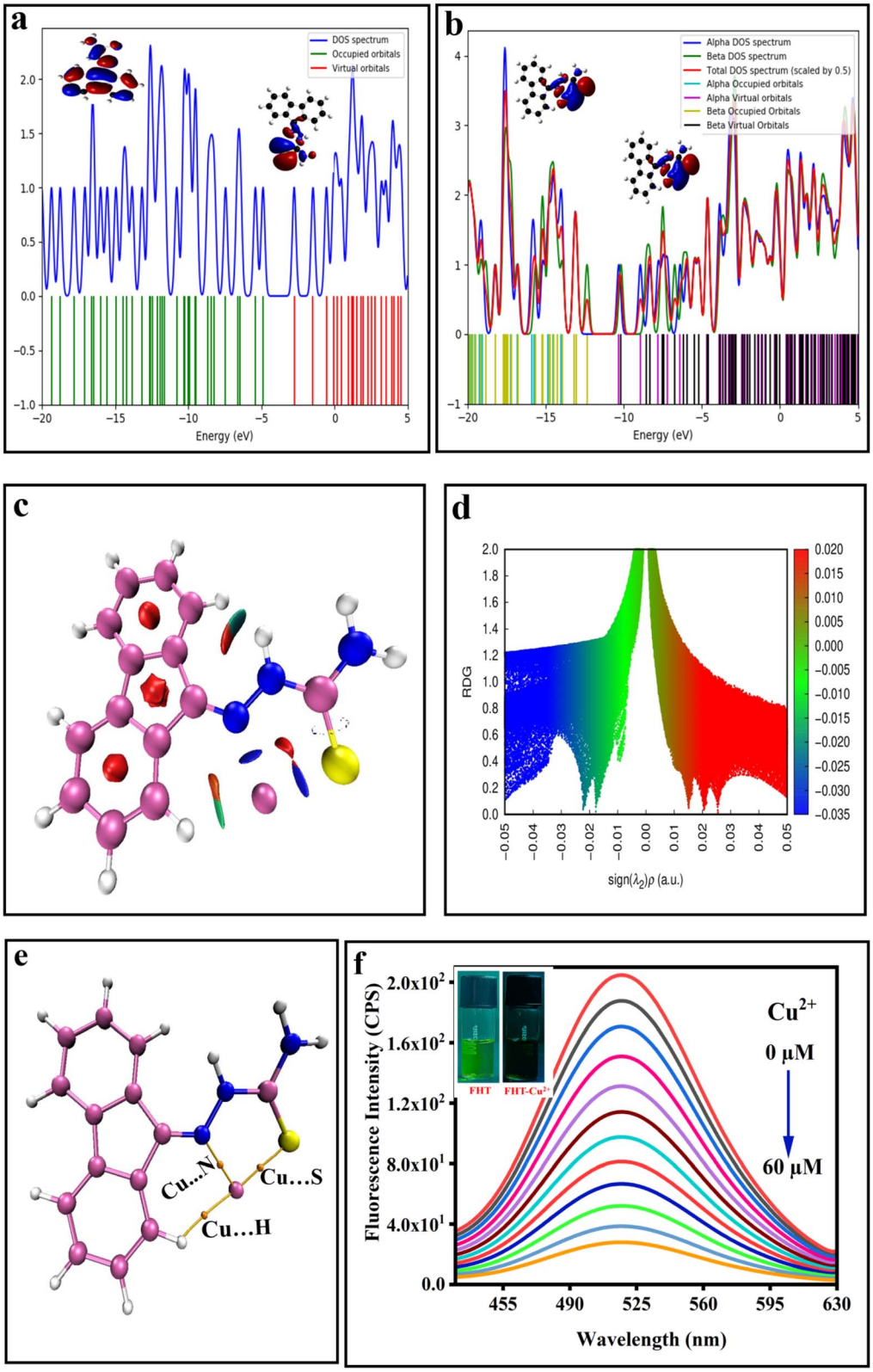

Fig. 4 DOS spectrum of the FHT sensor and FHT–Cu^{2+} complex (a and b). 3D and 2D NCI representations of the FHT–Cu^{2+} complex (c and d). QTAIM analysis of the FHT–Cu^{2+} complex (e). Emission spectrum of the FHT sensor for detection of Cu^{2+} in industrial effluents (f).

6.3. Development of logic gate systems using the FHT sensor

The observed variations in the fluorescence behavior of the **FHT** sensor suggest its potential application in the design and development of molecular logic devices.[62,63] In molecular logic systems, fluorescence signals are used to translate chemically encoded information. To examine the molecular logic behavior of the **FHT** sensor, a circuit was designed using a combination of NOT, AND, NAND, and OR gates, in which water (input-1) and Cu^{2+} (input-2) acted as the respective input signals (Fig. S7). Exposure of the **FHT** sensor to water was observed to result in an increase in fluorescence intensity, which was designated as an output of "1." In contrast, when both inputs (H_2O and Cu^{2+}) were either present or absent at the same time, the fluorescence intensity was reduced, leading to the output "0." A resulting truth table was constructed to match the expected functions of logic gates, thus demonstrating the potential of the **FHT** sensor for applications in molecular electronics (Table S4).

7. Conclusion

The **FHT** sensor was successfully synthesized in good yield, and its photophysical properties were systematically characterized. A bathochromic shift of 72 nm was measured for the **FHT** sensor from 440 nm in pure DMF to 512 nm at 90% water content, which indicates that the observed photophysical behavior arises from aggregation-induced emission (AIE) and the formation of J-aggregates. These photoluminescence properties were utilized to develop the **FHT** sensor for the detection of Cu^{2+} with high selectivity and sensitivity. The **FHT** sensor exhibited a limit of detection of 82 nM and a quenching efficiency of 97%. Spectroscopic analyses, including ^{1}H NMR and FTIR titrations, led to the identification of non-covalent interactions between the **FHT** sensor and Cu^{2+}. The selectivity of the **FHT** sensor was determined from interference studies for the detection of Cu^{2+} with other competing analytes, under different pH values and temperature conditions. Investigations on the photostability and response time indicate that the **FHT** sensor has high stability and provides fast and reliable sensing performance. Theoretical investigations, such as FMO and DOS calculations, showed the reduction of the HOMO–LUMO energy separation, as well as the emergence of new virtual orbitals, indicating the high sensitivity of the **FHT** sensor towards Cu^{2+}. The existence and importance of non-covalent interactions in the **FHT**–Cu^{2+} system were further validated by NCI and QTAIM calculations, with the bond critical point parameters demonstrating their role in the sensing mechanism. These findings demonstrate the effective use of **FHT** sensor for Cu^{2+} detection and validate its suitability for use in the environmental and industrial monitoring of Cu^{2+}. This sensor can also be applied for forensic studies and in the design of molecular logic-gate systems.

Conflicts of interest

There are no conflicts to declare.

Data availability

The supporting data have been provided as part of the supplementary information (SI). Supplementary information is available. See DOI: https://doi.org/10.1039/d6ra02022d.

Acknowledgements

The authors extend their appreciation to the University Higher Education Fund for funding this research work under the Research Support Program for Central Labs at King Khalid University through the project number CL/Health/2.

References

1 L. M. Wickham and R. Giri, Transition metal (Ni, Cu, Pd)-catalyzed alkene dicarbofunctionalization reactions, *Acc. Chem. Res.*, 2021, **54**, 3415–3437.
2 A. T. Aron, K. M. Ramos-Torres, J. A. Cotruvo Jr and C. J. Chang, Recognition-and reactivity-based fluorescent probes for studying transition metal signaling in living systems, *Acc. Chem. Res.*, 2015, **48**, 2434–2442.
3 J. Xu, H. Zhou, Y. Zhang, Y. Zhao, H. Yuan, X. He, *et al.*, Copper nanoclusters-based fluorescent sensor array to identify metal ions and dissolved organic matter, *J. Hazard. Mater.*, 2022, **428**, 128158.
4 L. Zeng, E. W. Miller, A. Pralle, E. Y. Isacoff and C. J. Chang, A Selective Turn-On Fluorescent Sensor for Imaging Copper in Living Cells, *J. Am. Chem. Soc.*, 2006, **128**, 10–11.
5 Y. Gao, X. Pan, S. Xu, Z. Liu, J. Wang, K. Yu, *et al.*, Fluorescence-enhanced microfluidic sensor for highly sensitive in-situ detection of copper ions in lubricating oil, *Mater. Des.*, 2020, **191**, 108693.
6 G. Hennrich, W. Walther, U. Resch-Genger and H. Sonnenschein, Cu(II)- and Hg(II)-Induced Modulation of the Fluorescence Behavior of a Redox-Active Sensor Molecule, *Inorg. Chem.*, 2001, **40**, 641–644.
7 S. C. Dodani, S. C. Leary, P. A. Cobine, D. R. Winge and C. J. Chang, A Targetable Fluorescent Sensor Reveals That Copper-Deficient SCO1 and SCO2 Patient Cells Prioritize Mitochondrial Copper Homeostasis, *J. Am. Chem. Soc.*, 2011, **133**, 8606–8616.
8 X. Wang, P. Li, W. Zhang and B. Tang, Recent Advances in Fluorescence Imaging of Bioactive Molecules in Neurons and in Vivo, *Chin. J. Anal. Chem.*, 2019, **47**, 1537–1548.
9 A. Akhuli, N. Preeyanka, D. Chakraborty and M. Sarkar, Turn-Off Detection of Reactive Oxidative Species and Turn-On Detection of Antioxidants Using Fluorescent Copper Nanoclusters, *ACS Appl. Nano Mater.*, 2022, **5**, 5826–5837.
10 P. Verwilst, K. Sunwoo and J. S. Kim, The role of copper ions in pathophysiology and fluorescent sensors for the detection thereof, *Chem. Commun.*, 2015, **51**, 5556–5571.
11 R. Deng, Y. Gao, S. Zhao, Y. Li, S. He, Y. Gao, *et al.*, Near-infrared II excited off-on fluorescent probe for molecular imaging of copper ions in Wilson disease, *Sens. Actuators, B*, 2025, **444**(Part 2), 138408.

12 B. Wang, J. Shi, W. Zhai, L. Jiang, Y. Ma, Z. Zhang, *et al.*, Construction of a bifunctional near-infrared fluorescent probe for visualization of copper (II) ions and amyloid-β aggregates in Alzheimer's disease, *Sens. Actuators, B*, 2025, **423**, 136767.

13 J. Chen, R. Luo, S. Li, J. Shao, T. Wang, S. Xie, *et al.*, A novel NIR fluorescent probe for copper (II) imaging in Parkinson's disease mouse brain, *Chem. Sci.*, 2024, **15**, 13082–13089.

14 J. Zhu, M. E. Graziotto, V. Cottam, T. Hawtrey, L. D. Adair, B. G. Trist, *et al.*, Near-infrared ratiometric fluorescent probe for detecting endogenous Cu^{2+} in the brain, *ACS Sens.*, 2024, **9**, 2858–2868.

15 S. M. Wazir and I. Ghobrial, Copper deficiency, a new triad: anemia, leucopenia, and myeloneuropathy, *J Community Hosp Intern Med Perspect*, 2017, **7**, 265–268.

16 F. Cheng, G. Peng, Y. Lu, K. Wang, Q. Ju, Y. Ju, *et al.*, Relationship between copper and immunity: the potential role of copper in tumor immunity, *Front. Oncol.*, 2022, **12**, 1019153.

17 C. Hu, X. Shi, J. Zhou, Z. Yang, Z. Wang, L. Huang, *et al.*, Selective detection of copper (II) dynamics in living cells and mice with diverse metabolic dysfunction-associated steatotic liver disease using a turn-on bioluminescent probe, *J. Hazard. Mater.*, 2025, 138667.

18 S. Comber, G. Deviller, I. Wilson, A. Peters, G. Merrington, P. Borrelli, *et al.*, Sources of copper into the European aquatic environment, *Integr. Environ. Assess. Manage.*, 2022, **19**, 1031–1047.

19 M. Bakshi and A. Kumar, Applications of copper nanoparticles in plant protection and pollution sensing: Toward promoting sustainable agriculture, in *Copper Nanostructures: Next-Generation of Agrochemicals for Sustainable Agroecosystems*, Elsevier, 2022, pp. 393–413.

20 A. Alharbi, A. A. A. Sari, A. H. Alessa, R. M. Snari, H. H. Alsharief, I. S. S. Alatawi, *et al.*, High-sensitivity detection of copper ions in water via cellulose nanomaterial nano-antennas and DFT studies, *Chem. Eng. J. Adv.*, 2024, **20**, 100675.

21 P. Piyanuch, S. Wangngae, A. Kamkaew, W. Wattanathana, S. Wannapaiboon, S. Impeng, *et al.*, Ultrasensitive fluorogenic chemosensor based on ESIPT phenomenon for selective determination of Cu^{2+} ion in aqueous system and its application in environmental samples and biological imaging, *Dyes Pigm.*, 2022, **205**, 110532.

22 E. Pourbasheer, S. Morsali, S. Ansari, B. Mirtamizdoust, H. Vojoudi and M. R. Ganjali, Extraction of trace quantities of copper using novel modified magnetite nanoparticles for atomic absorption spectrometry analysis, *Curr. Anal. Chem.*, 2022, **18**, 907–913.

23 R. Daymond, S. L. Curtis, V. Mishra and N. B. Roberts, Assay in serum of exchangeable copper and total copper using inductively coupled plasma mass spectrometry (ICP-MS): development, optimisation and evaluation of a routine procedure, *Scand. J. Clin. Lab. Invest.*, 2020, **80**, 630–639.

24 M. E. del Castillo Busto, S. Cuello-Nunez, C. Ward-Deitrich, T. Morley and H. Goenaga-Infante, A fit-for-purpose copper speciation method for the determination of exchangeable copper relevant to Wilson's disease, *Anal. Bioanal. Chem.*, 2022, **414**, 561–573.

25 O. Özbek and Ö. Isildak, Potentiometric determination of copper (II) ions based on a porphyrin derivative, *J. Chin. Chem. Soc.*, 2022, **69**, 1060–1069.

26 E. Tesfaye, B. S. Chandravanshi, N. Negash and M. Tessema, Development of a new electrochemical method for the determination of copper (II) at trace levels in environmental and food samples, *RSC Adv.*, 2022, **12**, 35367–35382.

27 A. G. Gkouliamtzi, V. C. Tsaftari, M. Tarara and G. Z. Tsogas, A low-cost colorimetric assay for the analytical determination of copper ions with consumer electronic imaging devices in natural water samples, *Molecules*, 2023, **28**, 4831.

28 D. Mohanasundaram, R. Bhaskar, N. Lenin, K. Nehru, G. Rajagopal, G. G. V. Kumar, *et al.*, A simple triphenylamine based turn-off fluorescent sensor for copper (II) ion detection in semi-aqueous solutions, *J. Photochem. Photobiol., A*, 2022, **427**, 113850.

29 J. S. Deb Roy, M. Deb, M. H. Sanfui, S. Roy, A. Dutta, P. K. Chattopadhyay, *et al.*, Light-emitting redox polymers for sensing and removal-reduction of Cu (II): roles of hydrogen bonding in nonconventional fluorescence, *ACS Appl. Polym. Mater.*, 2022, **4**, 1643–1656.

30 G. Huang, X. Luo, W. Lin, W. Tang, T. Yue, J. Wang, *et al.*, Carbon dots based multicolor fluorescence sensor for ratiometric and colorimetric dual-model detection of Cu^{2+}, *Dyes Pigm.*, 2022, **203**, 110381.

31 H. Zhang, Y. Li, H. Lu and F. Gan, A ratiometric fluorescence and colorimetric dual-mode sensing platform based on sulfur quantum dots and carbon quantum dots for selective detection of Cu^{2+}, *Anal. Bioanal. Chem.*, 2022, **414**, 2471–2480.

32 K. Wechakorn, U. Eiamprasert, J. Masoongnoen, A. Tantipanjaporn, P. Surawatanawong, P. Kanjanasirirat, *et al.*, A highly sensitive and selective rhodamine-semicarbazide based fluorescent sensor for Cu^{2+} detection in real water samples and fluorescence bioimaging in HepG2 cells, *Talanta*, 2024, **270**, 125530.

33 Y. He, H. Wang, X. Fang, W. Zhang, J. Zhang and J. Qian, Semicarbazide-based fluorescent probe for detection of Cu^{2+} and formaldehyde in different channels, *Spectrochim. Acta, Part A*, 2023, **299**, 122818.

34 M. Sahu, A. Kumar Manna, K. Rout, J. Mondal and G. K. Patra, A highly selective thiosemicarbazone based Schiff base chemosensor for colorimetric detection of Cu^{2+} and Ag^{+} ions and turn-on fluorometric detection of Ag^{+} ions, *Inorg. Chim. Acta*, 2020, **508**, 119633.

35 X. Bi, W. Hao, H. Liu, X. Chen, M. Xie, Y. Wang, *et al.*, Water-soluble host-guest fluorescent systems based on fluorophores and cucurbiturils with AIE or ACQ effects, *Dyes Pigm.*, 2021, **189**, 109267.

36 Y. Hong, J. W. Y. Lam and B. Z. Tang, Aggregation-induced emission: phenomenon, mechanism and applications, *Chem. Commun.*, 2009, 4332–4353.

37 K. Khurshid, S. A. Shahzad, M. A. Assiri, A. Shabbir, T. Javid and H. Irshad, Highly sensitive AIEE active fluorescent probe

for detection of deferasirox: extensive experimental and theoretical studies, *RSC Adv.*, 2024, **14**, 21682–21691.

38 A. Shabbir, S. A. Shahzad, A. Y. A. Alzahrani, Z. A. Khan, M. Yar and W. Rauf, A Multimode fluorescent sensor for sequential detection of Cu2+ and cysteine as well as pH sensor with real sample Applications: Extensive experimental and DFT studies, *Spectrochim. Acta, Part A*, 2025, **327**, 125414.

39 A. Shabbir, S. A. Shahzad, M. A. Assiri, Muqadas, I. Mustafa and W. Rauf, Synthesis and construction of aggregation induced emission based sensor for colorimetric multiphase sequential sensing of Al^{3+} and CN^{-} with real sample applications: Development of efficient vapor phase pH sensor, *J. Mol. Liq.*, 2025, **430**, 127706.

40 Y. Zhang, S. Yuan, P. Liu, L. Jing, H. Pan, X.-K. Ren, *et al.*, J-aggregation induced emission enhancement of BODIPY dyes via H-bonding directed supramolecular polymerization: the importance of substituents at boron, *Org. Chem. Front.*, 2021, **8**, 4078–4085.

41 S. Saeed, K. Khurshid, M. A. Assiri, A. Shabbir and S. A. Shahzad, Highly sensitive colorimetric and fluorescence "Turn On" sensing of hydrazine via restriction in intramolecular vibrations of AIEE active fluorophore, *Dyes Pigm.*, 2025, **239**, 112813.

42 A. Majeed, S. A. Shahzad, M. A. Assiri, K. O. Khan, H. Rabale and A. Shabbir, Highly selective and efficient AIEE active fluorescence probe for the detection of doxycycline in biological and environmental samples with extensive DFT support, *Spectrochim. Acta, Part A*, 2025, **331**, 125802.

43 L. Wang, Y. Shen, M. Yang, X. Zhang, W. Xu, Q. Zhu, *et al.*, Novel highly emissive H-aggregates with aggregate fluorescence change in a phenylbenzoxazole-based system, *Chem. Commun.*, 2014, **50**, 8723–8726.

44 S. Ma, Y. Liu, J. Zhang, B. Xu and W. Tian, Polymorphism-Dependent Enhanced Emission in Molecular Aggregates: J-Aggregate versus X-Aggregate, *J. Phys. Chem. Lett.*, 2020, **11**, 10504–10510.

45 M. J. Frisch, G. W. Trucks, H. B. Schlegel, G. E. Scuseria, M. A. Robb and J. R. Cheeseman, *et al*, *Gaussian 09, Revision D.01*, Gaussian, Inc., Wallingford CT, 2013.

46 Susheel, A. S. Alsubaie, M. Ahmed, S. S. Malhotra, Asha, M. K. Gupta, *et al.*, DFT and TDDFT studies on π-conjugated ligands for copper sensing: analyzing electronic structures and optical performance, *J. Mol. Model.*, 2025, **31**, 306.

47 G. Paytakov, T. Dinadayalane and J. Leszczynski, Toward selection of efficient density functionals for van der Waals molecular complexes: comparative study of C–H$\cdots$ π and N–H$\cdots$ π interactions, *J. Phys. Chem. A*, 2015, **119**, 1190–1200.

48 C. E. Check, T. O. Faust, J. M. Bailey, B. J. Wright, T. M. Gilbert and L. S. Sunderlin, Addition of polarization and diffuse functions to the LANL2DZ basis set for p-block elements, *J. Phys. Chem. A*, 2001, **105**, 8111–8116.

49 S. A. Rupa, M. A. M. Patwary, W. E. Ghann, A. Abdullahi, A. R. Uddin, M. M. Mahmud, *et al.*, Synthesis of a novel hydrazone-based compound applied as a fluorescence turn-on chemosensor for iron (III) and a colorimetric sensor for copper (II) with antimicrobial, DFT and molecular docking studies, *RSC Adv.*, 2023, **13**, 23819–23828.

50 T. Azam, Z. Ahmad, S. Sarfaraz, S. Mahmood and K. Ayub, Theoretical insights of 2D carbon nitride (C_3N) as a highly selective sensor for volatile analytes, *Sci. Rep.*, 2026, **16**, 5780.

51 T. Lu and F. Chen, Multiwfn: A multifunctional wavefunction analyzer, *J. Comput. Chem.*, 2012, **33**, 580–592.

52 W. Humphrey, A. Dalke and K. Schulten, VMD: Visual molecular dynamics, *J. Mol. Graphics*, 1996, **14**, 33–38.

53 B. Carlotti, R. Flamini, I. Kikaš, U. Mazzucato and A. Spalletti, Intramolecular charge transfer, solvatochromism and hyperpolarizability of compounds bearing ethenylene or ethynylene bridges, *Chem. Phys.*, 2012, **407**, 9–19.

54 N. Pandey, N. Tewari, S. Pant and M. S. Mehata, Solvatochromism and estimation of ground and excited state dipole moments of 6-aminoquinoline, *Spectrochim. Acta, Part A*, 2022, **267**, 120498.

55 N. J. Hestand and F. C. Spano, Molecular Aggregate Photophysics beyond the Kasha Model: Novel Design Principles for Organic Materials, *Acc. Chem. Res.*, 2017, **50**, 341–350.

56 A. P. Deshmukh, D. Koppel, C. Chuang, D. M. Cadena, J. Cao and J. R. Caram, Design Principles for Two-Dimensional Molecular Aggregates Using Kasha's Model: Tunable Photophysics in Near and Short-Wave Infrared, *J. Phys. Chem. C*, 2019, **123**, 18702–18710.

57 H. Yang, Y. Wu and F. Tian, A Fluorescent Sensor for Cu^{2+} Ion with High Selectivity and Sensitivity Based on ICT and PET, *J. Fluoresc.*, 2019, **29**, 1153–1159.

58 M. Guin, S. Halder, S. Chatterjee and S. Konar, Synthesis, X-ray crystal structure of Cu (II) 1D coordination Polymer: In View of Hirshfeld surface, FMO, Molecular electrostatic potential (MEP) and Natural Bond orbital (NBO) analyses, *J. Mol. Struct.*, 2022, **1270**, 133949.

59 A. Sharma, M. S. Khan, M. Husain, M. S. Khan and A. Srivastava, Sensing of CO and NO on Cu-doped MoS 2 monolayer-based single electron transistor: A first principles study, *IEEE Sens. J.*, 2018, **18**, 2853–2860.

60 M. Malček and M. N. D. Cordeiro, A DFT and QTAIM study of the adsorption of organic molecules over the copper-doped coronene and circumcoronene, *Phys. E*, 2018, **95**, 59–70.

61 N. Ahmed, J. Liu, X. Xu, A. Hussain, A. Mustafai, M. Yar, *et al.*, An activatable NIR turn-on fluorescent probe for copper (II) ion and live cell imaging, *Sci. Rep.*, 2024, **14**, 19068.

62 M. Yuan, W. Zhou, X. Liu, M. Zhu, J. Li, X. Yin, *et al.*, A Multianalyte Chemosensor on a Single Molecule: Promising Structure for an Integrated Logic Gate, *J. Org. Chem.*, 2008, **73**, 5008–5014.

63 Q. Sajid, A. Shabbir, A. M. Khan, M. A. Assiri, W. Rauf and S. A. Shahzad, Synthesis and development of indanone as AIE based fluorescent probe for ultrasensitive detection of 4-nitroaniline in solid and vapor phase, *Microchem. J.*, 2025, **219**, 116055.